The effect of surface states accumulation on photo-electrochemical performances of $Bi_{24}Fe_2O_{39}$ grown by supersonic beams

Skerxho Osmani [a], Enrico Scattolin [b], Michele Vergari [a], Alberto Gasparotto [b,c], Gian Andrea Rizzi [b,c,**], Luca Gavioli [a,*]

[a] Interdisciplinary Laboratories for Advanced Materials Physics (i-LAMP) & Dipartimento di Matematica e Fisica, Università Cattolica del Sacro Cuore, via della Garzetta 46, 25131, Brescia, Italy
[b] Department of Chemical Sciences – Padova University, Via Marzolo, 1, 35131, Padova, Italy
[c] CNR-ICMATE and INSTM, Department of Chemical Sciences, Padova University, 35131, Padova, Italy

A B S T R A C T

Holes accumulation on the surface of bismuth ferrite oxides (BFO) photoanodes for photoelectrochemical (PEC) water splitting (WS) is one of the major issues limiting the overall cell efficiency. However, among the various BFO crystal structures, no evidence of this mechanism has been reported for $Bi_{24}Fe_2O_{39}$, a scarcely investigated phase. Herein we characterize the morphological, structural and PEC properties of 100 nm thick nanogranular films of a $Bi_{24}Fe_2O_{39}$ single phase synthesized by supersonic cluster beam deposition. The films were tested as photoanodes for the WS reaction in KOH and Na_2SO_4 + Na_2SO_3 electrolytes. The PEC data provide direct evidence of holes accumulation on the surface of the material with increasing applied biases. The interesting performances of this material at low biases suggest a possible use as photocatalyst under visible light irradiation.

1. Introduction

The quest for low-cost methods to produce renewable energy vectors is a global scientific and technological challenge. In this context, photoelectrochemical (PEC) water splitting represents a promising route, potentially allowing the large-scale generation of green hydrogen directly from solar energy. The process, involving an electrochemical cell in which H_2 and O_2 are produced at the cathode and anode respectively, requires a photoactive semiconductor at one or both electrodes, capable of triggering the photogeneration of electron/hole pairs and to efficiently deliver such species to the surface active sites, driving the different steps involved in the two required half-reactions [1, 2].

Ternary metal oxides (TMOs) based on metallic elements such as molybdenum [3], vanadium [4], tungsten [5–7], niobium [8] and bismuth [9] feature band gaps and band edge positions suitable to potentially achieve high PEC efficiency [10], but present major limitations, e. g. the high recombination rate of charge carriers, frequently due also to the presence of surface states (SS) [10]. The role and physical mechanism of recombination and injection can be described by the reaction

kinetic constants, i.e. krec (recombination) and kinj (injection) [11], measured through intensity modulated photocurrent spectroscopy (IMPS) [12–15]. Most important, k_{inj} and k_{rec} depend on the TMO phase [16,17], stoichiometry [17] and grain size, highlighting the role of synthesis methods to properly engineer such materials [18].

TMOs obtained by chemical vapor (CVD) [19,20], atomic layer deposition (ALD), and magnetron sputtering (MS) require time-consuming steps [12] to achieve the targeted stoichiometry. Furthermore, current TMO PEs produced by CVD [19,20], sol-gel [21] and physical synthesis methods [16,22] such as electrodeposition [23], electron beam evaporation [24] and flame spray pyrolysis [25] usually produce mixed BFO phases and do not allow to explore the kinj and krec dependence on the PE nanostructure morphology below 50 nm grain size and thickness.

Among TMOs and, specifically, bismuth based ternary oxides, the efficacy of bismuth ferrite oxides (BFO) has been investigated given their appropriate band gap for visible light absorption (2.0–2.8 eV) [26]. Therefore, different BFO crystal structures, such as $BiFeO_3$ [19,21,23, 24] (perovskite) and $Bi_2Fe_4O_9$ [27,28] (mullite) have been synthesized and tested as photoanodes. In this context, no studies are available on

---

* Corresponding author.
** Corresponding author. Department of Chemical Sciences – Padova University, Via Marzolo, 1, 35131, Padova, Italy.
E-mail addresses: gianandrea.rizzi@unipd.it (G.A. Rizzi), luca.gavioli@unicatt.it (L. Gavioli).

the use of phase-pure $Bi_{24}Fe_2O_{39}$ photoanodes and holes/SS accumulation mechanism, such a BFO having been reported only as impurity of other majority phases [20] or as suspended powdered photocatalyst [29]. Studying the chemical-physical characteristics of photoanodes selectively consisting of this phase can provide a better fundamental understanding of phenomena involved in PEC water splitting, potentially allowing to develop more efficient BFO systems.

In this work, BFO nanoparticles (NPs) were generated using pulsed micro-plasma cluster source (PMCS) technique and deposited on a fluorine-doped tin oxide (FTO) glass substrate with supersonic cluster beam deposition (SCBD). The combination of the PMCS with SCBD (PMCS-SCBD) allows the synthesis of nanogranular thin films with tunable stoichiometries changing the elemental composition of a suitable target material [30–33]. The main advantages of SCBD, provided by the soft landing regime that maintains the original NP structure and shape [34,35], include control of grain size (typically in the range 1–15 nm) and film thickness, achieving optimal adhesion to the substrate avoiding solvents or contaminants. This work describes for the first time the PMCS-SCBD synthesis of the phase-pure $Bi_{24}Fe_2O_{39}$ thin films on FTO, along with their chemico-physical and PEC characterization, focusing on the utilization of this TMO as photoanode in the WS process. We provide direct experimental evidence, obtained by IMPS, of SS accumulation on the electrode surface, complicating its use as photoanode at relatively high biases.

2. Methods

2.1. Synthesis

A supersonic beam of nanoparticles (NPs) is provided by a high pressure (35–50 bar range) spark Helium plasma ablation of a BiFe rod (50:50 atomic concentration). A high voltage 800–950 V) synchronized with the pulsed He injection is applied to the rod at 3 Hz frequency, thus generating a NPs-gas mixture (average pressure 10^{-3} mbar) that is extracted from the condensation chamber through a nozzle (Fig. S1). The beam is subsequently focused by a set of aerodynamic lenses and a skimmer is used to select its central section. The NPs are deposited at 10^{-6} mbar directly on the substrates. A quartz microbalance controls in real time the coating thickness. The films are formed by exposing any substrate the NP beam and the film thickness is determined by the deposition time and beam rate.

The films were deposited simultaneously onto FTO-coated glass (FTO thickness = 550 nm; glass thickness = 2 mm) and Si(111) substrates, and subsequently analyzed either as such or after an annealing treatment in air for 2 h at 500 °C. The samples deposited on FTO were used for the structural, optical and electrochemical measurements while the samples on Si(111) were used to characterize the NPs beam building blocks and to measure the thickness of the deposited layers.

2.2. Physical characterization

Atomic force microscopy (AFM) data (2 μm × 2 μm area at 1024 x 1024 pixels, and 10 μm × 10 μm at 2048 x 2048 pixel) were acquired with a Park NX10 in noncontact mode employing PPP-NCHR50 tips (NanoAndMore GMBH) and the images were processed with Gwyddion software. Due to the soft landing regime typical of SCBD [34,35], NPs maintain the original structure and shape after deposition. Hence the NP size (assuming a spherical shape) may be obtained by measuring with AFM the maximum height of isolated NPs with respect to a flat substrate (in this work Si(111), avoiding tip convolution effects) [36]. After removing a first order background, NPs were identified as regions with height deviations from the baseline exceeding 3 times the Si(111) root mean square (RMS) roughness (0.23 nm ± 0.01 nm). The NP height was taken as the maximum vertical value of each isolated region. For the histogram distribution, a total of 1900 NPs were used. The film thickness after deposition was determined by measuring the edge of the film with

respect to the Si(111) substrate.

Film composition was investigated by X-ray photoelectron spectroscopy (XPS) using a non-monochromatic Al X-ray source (incident photon energy 1486.6 eV) and a Phoibos 100 SPECS analyzer at 20 eV pass energy. Data were acquired with 0.1 eV/step for a 100 nm thick BFO layer deposited onto the Si and the FTO substrates. The photoelectron sampling depth for the elements composing the film is up to 5 nm [37]. The data were analyzed using CasaXPS software, by employing a Shirley background and modelling each metal component by a LA(50) asymmetric curve and GL(50) peaks for the other components. All spectra were corrected for charging by assigning a binding energy (BE) of 284.8 eV to the major carbon 1s peak.

Optical data were acquired in 250–2500 nm range with a PerkinElmer Lambda950 spectrophotometer equipped with an integrating sphere. The optical absorption coefficient α was calculated from the direct transmittance T and specular reflectance R (reported in Fig. S2 of the supporting information) using the following relation to include also multiple internal reflections [38,39]:

$$\alpha(E) = \frac{1}{d} ln \left[\frac{(1-R)^2}{2T} + \sqrt{\frac{(1-R)^4}{4T^2} + R^2} \right] \tag{1}$$

The optical band gap was obtained with the following relation, applicable for direct transitions in polycrystalline semiconductors [38, 40] and recently suggested in a comprehensive review of the band gap determination [39]:

$$\alpha^2 \propto (h\nu - E_g) \tag{2}$$

where hv is the incident photon energy and E_g the band gap. E_g is found at the photon energy at which α = 0.

X-ray diffraction (XRD) measurements were performed in a glancing incidence mode ($\vartheta_i = 1.0°$) using a Bruker AXS D8 Advance Plus diffractometer, equipped with a Gobel mirror and a CuKα X-ray source (λ = 1.54051 Å). The pattern was collected in the 15–65° 2ϑ range with a resolution of 0.06°/step and an acquisition time of 5 s/step.

2.3. PEC characterization

Photoelectrocatalytic activity tests were performed at room temperature by an integrated system consisting of a Zennium-PRO and a PP212 unit from Zahner GmbH, coupled with an optical bench equipped with a Zahner photoelectrochemical cell. FTO-supported BFO systems were used as working electrodes, whereas a Pt coil and an Ag/AgCl electrode ($E°_{Ag/AgCl}$ = 0.199 V) were used as counter- and reference electrode, respectively. The electrical contact was made by sticking a stripe of copper tape on the edge of FTO conductive face. Linear sweep voltammetry (LSV; scan rate = 5 mv/s) measurements were performed in 0.1 M Na_2SO_4 + 0.1 M Na_2SO_3 aqueous solution (pH = 8.6) and in KOH 0.1 M (pH = 13.05). IMPS analyses were carried out applying a LED frequency between 10000 and 0.05 Hz with a 15 % of light intensity modulation. The white light intensity was set at 50 mW/cm^2. Electrochemical impedance spectroscopy (EIS) data were acquired from 100 mHz to 10 kHz with a potential modulation of 5 mV. Mott-Schottky plots were obtained between 0.4 and 1.2 V *vs.* RHE, with 0.05 V/step. The capacitance value (C_{sc}) was obtained by fitting each spectrum with an equivalent circuit model (ECM) as reported in Fig. S4. The flatband potential (V_{FB}) was measured by fitting the linear part of $1/C_{sc}^2$ and finding the intercept with the voltage axis, using the equation [13–15]:

$$\frac{1}{C_{sc}^2} = \frac{2}{(\varepsilon_0 \varepsilon_r e N_D)} \left(V - V_{FB} - \frac{(K_B T)}{e} \right) \tag{3}$$

where C_{SC} is the capacitance of the semiconductor ($1/C_H^2$, capacitance of the double layer, is considered negligible), ε_0 is the permittivity of free space, ε_r is relative permittivity of the target material, e is the electron charge, and k_B is the Boltzmann constant. The majority carrier

concentration (N_D) was obtained from the slope of the linear part of $1/C_{SC}^2$.

The incident photon-to-current conversion efficiency (IPCE) is a measure of the ratio of the photocurrent (converted to an electron transfer rate) vs. the rate of incident photons (converted from the calibrated power of a light source) as a function of wavelength. The IPCE (%) considers the efficiencies for photon absorption/charge excitation and separation ($\eta_{e/h}$), charge transport within the solid to the solid–liquid interface transport (η_{tr}), and interfacial charge transfer across the solid–liquid interface (η_{CT}). The IPCE was measured in the potential interval 0.4–1.4 V vs. RHE, and the values were calculated as follows [13–15]:

$$IPCE(\%) = \frac{(1240\, j)IPCE}{P\lambda} \qquad (4)$$

where 1240 is expressed in eV nm, j is the photocurrent density, λ is the incident light wavelength, and P is the incident light power density for each wavelength. Measurements were obtained by using fourteen different LED light sources with wavelengths between 365 and 810 nm. Each source light intensity was measured in real time by a photodiode during LSV acquisition. The APCE was calculated from absorbance measurements (Fig. S2C) from the following equation [13–15]:

$$APCE(\%) = \frac{IPCE}{\left(1 - 10^{-A}\right)} \qquad (5)$$

where the absorbance is defined as A=1-R-T. Finally, the applied bias photoconversion efficiency (ABPE) and (FF) values were obtained according to the following equations:

$$ABPE(\%) = \Delta j_{\times} \frac{(1.23 - V_{Bias})}{P} \times 100 \qquad (6)$$

$$FF(\%) = \Delta j_{max} \times \frac{(1.23 - V_{max})}{j_{1.23} \times (1.23 - V_{on})} \times 100 \qquad (7)$$

where Δj_{max} and V_{max} correspond to the photocurrent density and applied bias values giving the highest ABPE, and V_{on} to the potential value for the photocurrent onset. The ABPE value together with FF represent the photoelectrode efficiency to convert light into electrical power. In particular, the FF represents the "squareness" of the photoelectrode current-voltage (IV) curve. It also corresponds to the area of the largest rectangle that fits within the IV curve.

3. Results and discussion

The electrode growth through SCBD takes place by the aggregation of the NPs landing on the substrate from the beam. In the ballistic regime typical of SCBD, the individual NP size determines the roughness of the films, which may have an impact on electrochemical performances. It is worth highlighting that NPs obtained through SCBD have never been reported earlier for this material. Hence a characterization of the as deposited NPs in terms of their morphology and particle size distribution is essential. A representative AFM image of sparse NPs on Si(111) is shown in Fig. 1a. The NPs are the brightest areas distinct from the substrate in red. While most of the features correspond to single NPs, there are also some agglomerated structures. As explained in the experimental section, the NPs maximum height corresponds to the NP diameter. The corresponding histogram, shown in Fig. 1b–is fitted by a log-normal distribution [41] centered at $x_0 = 3.7$ nm with a standard deviation of 1.2 nm, consistent with the ballistic deposition regime [42].

The films are grown by direct exposure of the FTO substrates to the beam and, after the annealing treatment, are employed as electrodes. Fig. 2a shows a typical AFM image of the as deposited layer on the FTO substrate. Due to the NP agglomeration and convolution with the tip radius, it is not possible to distinguish single NPs to determine a grain size with AFM. However, an analysis of images acquired in different sample regions reveals an RMS roughness of 16.2 ± 0.3 nm. Furthermore, the film thickness measured from the quartz microbalance during the deposition, assuming an average mass density between Fe and Bi, is 67 nm. However, the film height obtained by AFM on an edge of the same layer deposited simultaneously on the Si(111) substrate gives an actual thickness of 100 nm, indicating a porosity of 33 %. The AFM data acquired after the annealing process (see Fig. 2b) indicate a small increase of the RMS roughness to 16.6 ± 0.3 nm, while larger structures (bright areas) are appearing on the surface. These data suggest no appreciable variation in the surface roughness of the film after the thermal treatment.

The diffraction pattern for the thermally treated BFO layer deposited on Si(111), reported in Fig. 3 (black curve), showed peaks at $2\theta = 16.2$, 28.0, 31.7, 32.8, 46.1, 47.0, 54.1, 55.6 and 57.7° attributable, respectively, to reflections from (110), (201), (002), (220), (222), (400), (203), (421) and (402) planes of a tetragonal $Bi_{24}Fe_2O_{39}$ phase (powder diffraction file card 42–0201; space group P-421c; lattice parameters: a = b = 7.705 Å; c = 5.667 Å; $\alpha = \beta = \gamma = 90°$). The good matching between the experimental pattern and the database one, both in terms of peak positions and relative intensities, strongly supports the selective obtainment of the above-mentioned crystal structure, scarcely investigated in the literature and reported as phase-pure material only in some works [20,29,43–48]. The observed peaks match well with a very recent work which identifies the unit cell structure of $Bi_{24}Fe_2O_{39}$ [49]. The above reflections were detected even for the BFO layer deposited on FTO (Fig. 3, red curve), whose pattern also showed some additional peaks attributable to the underlying FTO substrate. The estimation of the $Bi_{24}Fe_2O_{39}$ crystal size for this sample yielded values of 32 ± 3 nm, very similar to the ones obtained on the corresponding Si(111) supported system.

Overall, such results indicate that the adopted PMCS/SCBD synthetic approach is transferable to different substrate materials. Furthermore,
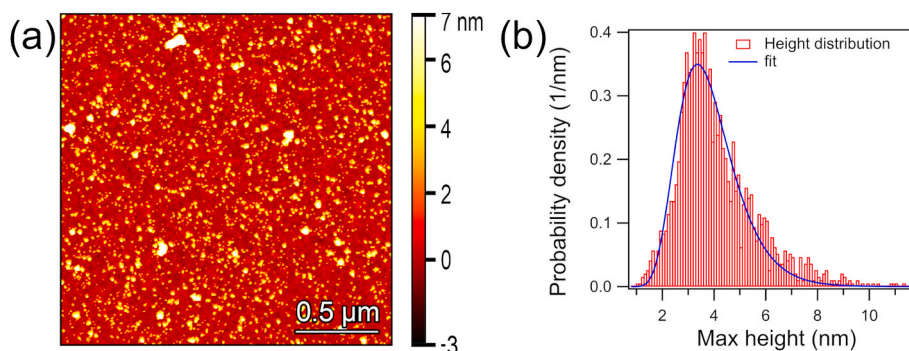

Fig. 1. (a) 2 µm × 2 µm AFM images of sparse NPs deposited on the Si(111) substrate to determine the NP size; (b) NPs height distribution revealing a log-normal distribution centered at 3.7 nm.
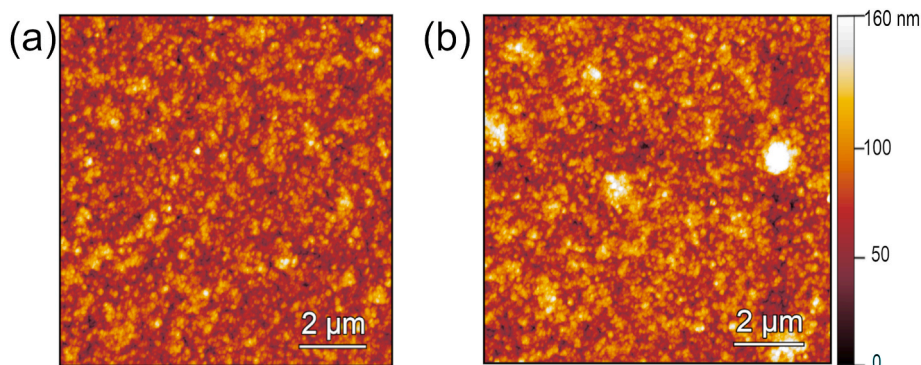
Fig. 2. 10 μm × 10 μm AFM images of a 100 nm thick BFO layer on FTO before (a) and after (b) the annealing process with the same color scale.
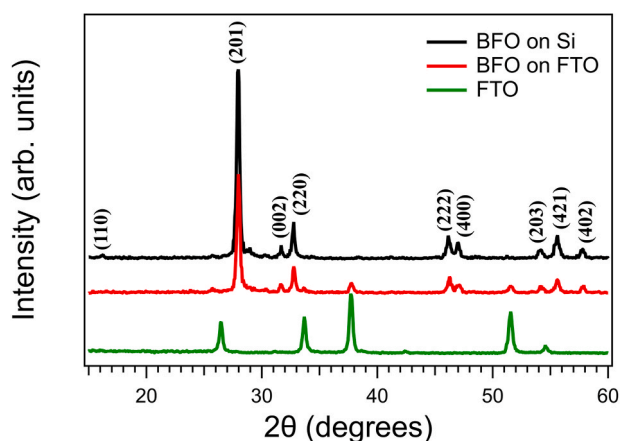

Fig. 3. XRD patterns of Si(111) and FTO-supported BFO layers after thermal treatment in air at 500 °C. For comparison, the spectrum of a bare FTO substrate is also displayed.

the crystal grain size obtained from XRD data, much larger than the main NP size obtained from the beam characterization, suggests that the annealing treatment induces a strong increase of NPs size.

As mentioned for the beam characterization conducted with AFM, it is also important to determine the stoichiometry of the film prior to the electrochemical tests. Fig. 4 shows typical Fe 2p, Bi 4f, O 1s and C 1s XPS core level spectra obtained on a 100 nm thick BFO layer deposited on Si (111), after the thermal treatment. BEs, FWHM values and peak areas are summarized in Table 1, while the relative atomic concentrations, obtained from the peak areas employing the sensitivity factors of CasaXPS, are reported in Table 2.

The Fe 2p spectra and pertaining peak deconvolution are shown in Fig. 4a. The deconvolution of Fe 2p line-shape is complex because the core holes generated by photoemissions, when a 3d electron is promoted to the 4s level, are coupling with the high-spin states of iron thus generating shake up satellite peaks [50]. The fitting process was carried out taking as an initial reference literature values for the binding energy (BE), areas and FWHM of the different components, the latter broadened to consider the use of a non-monochromatic XPS source. For iron oxides components, the reference parameters were defined by XPS measurements performed in situ on a pure Fe_2O_3 sample. Hence BEs, areas, and FWHM parameters of the Fe main component and satellites were constrained, and the fit was performed by exclusively varying the intensity of the principal components of $Fe^{3+}_{3/2}$ and $Fe^{2+}_{3/2}$ oxidation states. Shirley-type background was subtracted for both as prepared and post-annealed samples and the curve was fitted with a GL(50) component. The $Fe\ 2p_{3/2}$ and its shake-up component are identified at 709.8 eV and 713.8 eV BE for the Fe^{2+} oxidation state and at 711.1 eV and 718.5 eV BE for the Fe^{3+} oxidation state, respectively, close to values reported

for similar iron oxides [50,51]. The data show that both Fe^{2+} and the Fe^{3+} contributions are present in the film. The Bi 4f spectra and pertaining peak deconvolution are shown in Fig. 4b. The quantification of the doublet arising from the Bi spin-orbit splitting was achieved by employing a GL(50) lineshape, an energy separation of $\Delta = 5.7$ eV and an area ratio of 3:4, in accordance with the expected degeneracy ratio [50]. Fig. 4b exhibits Bi 4f with doublet peaks around 158.5 and 163.8 eV, corresponding to the Bi^{3+} oxidation state indicating the complete Bi oxidation. BEs, FWHM and peak areas for Bi are summarized in Table 1.

Fig. 4c and d shows the XPS spectra of the O 1s and C 1s core levels. In the oxygen region, the main feature is due to the BFO lattice oxygen contribution at 529.7 eV BE. Furthermore, three additional components are identified at 531.2 eV, 532.5 eV and 533.6 eV BE, corresponding to hydroxyl species, carbonates and chemisorbed water, respectively. In the C 1s spectrum, the main feature at 284.8 eV BE due to C–C bonds from adventitious aliphatic species, is accompanied by the C–O and O–CO contributions observed at 286.5 eV and 288.4, respectively. Compositional data in Table 2 indicate a Bi:Fe atomic ratio slightly higher than the one expected basing on XRD results, revealing a Bi enrichment at the film surface. Taking into account information provided by the analysis of O 1s and C 1s signals, such a result might be traced back to the formation of hydroxyl/carbonate bismuth-containing species in the outermost regions of the BFO film, arising from its interaction with atmospheric H_2O/CO_2 and promoting a partial Bi segregation towards the surface. A similar hypothesis is consistent with the formation of species such as $(BiO)_2CO_3$ and $(BiO)_4(OH)_2CO_3$ on the surface of the Bi_2O_3 nanostructures, reported in the literature [52,53].

Fig. 5a shows the valence band XPS spectrum in the range between −4 eV and 6.5 eV for the BFO sample before its use as photoelectrode (orange curve). The intercept of the linear extrapolations of the leading edge and the baseline (black lines) marks the positions of the valence band energy at 0.85 eV $\pm$ 0.06 eV. The same sample was analyzed after electrochemical measurements (green curve) confirming the value of the valence band (0.84 eV $\pm$ 0.11 eV). Fig. 5b shows α^2 as a function of the incident photon energy calculated from the direct transmittance T and specular reflectance R as described in the methods section. A linear fit of the slope of α^2 was performed in the range between 2.6 and 2.8 eV and from its intersection with the horizontal axis, we obtained Eg = 2.57 $\pm$ 0.04 eV. Transmittance and reflectance spectra of the sample after the electrochemical measurement do not show appreciable differences. Overall, such results indicate a good material stability upon electrochemical testing.

In Fig. 6 we report the main results of the PEC tests performed on a 100 nm thick $Bi_{24}Fe_2O_{39}$ film deposited on FTO. Fig. 6a shows the chopped light LSV results obtained in 0.1 M KOH (green curve) and 0.1 M Na_2SO_4 + 0.1 M Na_2SO_3 (pink curve). The LSV curves reported in Fig. 6b were obtained in the dark (yellow curve) and under continuous illumination (red curve) in 0.1 M Na_2SO_4 + 0.1 M Na_2SO_3. The corresponding photocurrent ($\Delta j = j_{light} - j_{dark}$), applied bias photoconversion efficiency (ABPE) curve and fill factor (FF), calculated according to
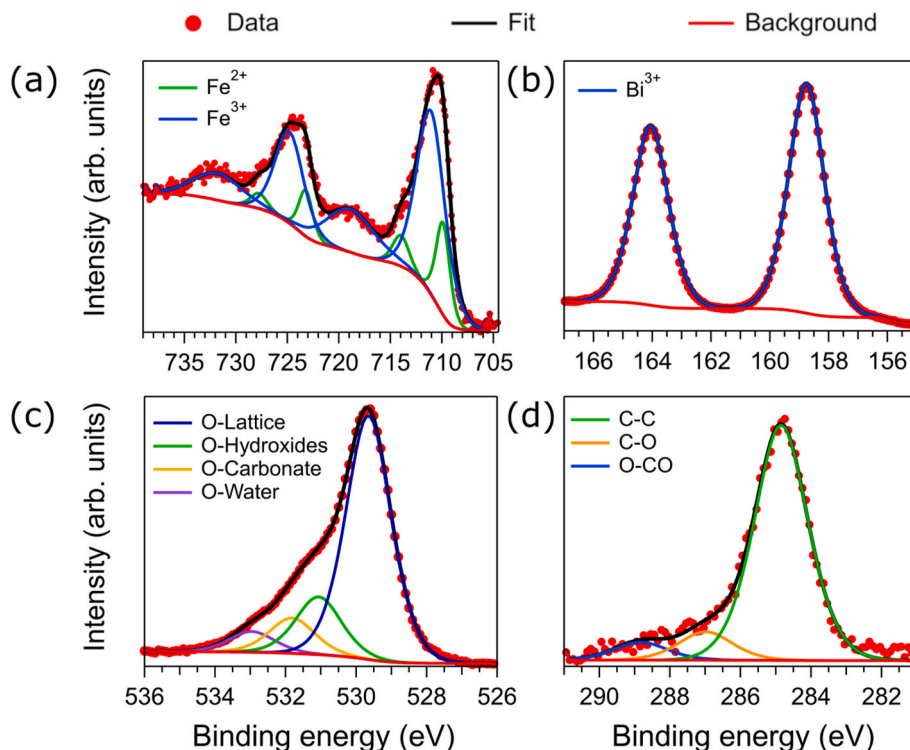
Fig. 4. XPS spectra (red dots) of BFO layer after the annealing treatment. The black line represents the fitted results after Shirley-type background subtraction (red curve). Deconvoluted spectral peaks are shown: (a) Fe^{2+} and Fe^{3+} peaks (green and blue curves, respectively) of Fe 2p; (b) Bi^{3+} peaks (blue curves) of Bi 4f; (c) lattice oxygen (blue curve), hydroxyl groups (green curve), carboxylic oxygen (orange curve) and chemisorbed water (purple) of O 1s; (d) adventitious C (green curve), C–O (orange curve) and C=O (blue curve) of C 1s.

Table 1

Deconvolution parameters of the Fe 2p, Bi 4f, O 1s and C 1s peaks for a 100 nm thick $Bi_{24}Fe_2O_{39}$ film after annealing. All the components were reproduced with a GL(50) lineshape.

Component	BE (eV)	FWHM (eV)	Area
Fe2+ 3/2	709.9	2.2	769
Fe2+ 3/2 S	713.9	2.6	308
Fe2+ 1/2	723.2	3.3	384
Fe2+ 1/2 S	727.7	5.9	1154
Fe3+ 3/2	711.1	2.3	3138
Fe3+ 3/2 S	718.9	2.8	1255
Fe3+ 1/2	724.8	3.0	1569
Fe3+ 1/2 S	731.8	5.2	785
Bi3+ 7/2	158.5	1.4	84775
Bi3+ 5/2	163.8	1.4	66124
O-Lattice	529.7	1.5	20254
O-Hydroxide	531.2	1.5	6139
O-Carbonate	532.5	1.5	2355
O-Water	533.6	1.5	500
C–C	284.8	1.7	3749
C–O	286.5	1.7	482
O–CO	288.4	1.7	265

Table 2

Relative atomic concentration of Bi, Fe, O and C of the surface of BFO film as deduced from XPS analysis.

Element	Bi	Fe	O	C
Concentration (%)	30.7	2.0	43.6	23.7

equations (6) and (7), are reported in the inset. Finally, Fig. 6c reports the Mott-Schottky (MS) plot obtained in $Na_2SO_4 + Na_2SO_3$ electrolyte, while Fig. 6d shows the IMPS normalized Nyquist plots recorded from

1.3 to 1.6 V vs RHE. We obtained a flat band potential value (0.39 V vs RHE) either from MS analysis (Fig. 5c) or from the square of the photocurrent very close to the published one for β-Bi_2O_3, characterized by a crystal structure identical to that of $Bi_{24}Fe_2O_{39}$ [54].

The measurements were performed in a $Na_2SO_4 + Na_2SO_3$ solution, due to the stable behavior as compared to NaOH or Na_2SO_4 electrolytes. The current instability for the latter electrolytes consisted in the shift of the open circuit potential (OCP) to higher or lower values depending on the applied polarization. For higher applied biases, the OCP was shifting upwards, and the original position was recovered only after application of cathodic biases.

Due to the low Fe/Bi ratio and the structure identical to that of β-Bi_2O_3, the rationalization of the observed behavior may be obtained by comparing to the PEC characterization of β-Bi_2O_3 [55]. In fact, the upward shift of OCP and Fermi level observed in β-Bi_2O_3 based photoanodes are attributed to the accumulation of holes on the surface [54]. This effect, limiting the catalytic activity for oxygen evolution, may be revealed by employing a good hole scavenger in the electrolyte. In fact, in Fig. 6a the chopped light LSVs acquired in the electrolyte containing Na_2SO_3 (hydrogen peroxide could not be used due to the presence of Fe ions) presents a photocurrent density which is more than twice the one obtained in 0.1 M KOH. This behavior is confirmed by the obtained FF value (22 %) which indicates a scarce efficiency of this photoelectrode to convert light into electrical power. The performance of the current electrodes is apparently lower than that obtained for powders of the same compound [49]. However, a specific current normalized to the actual material active surface and not to the geometrical electrode surface would provide a direct comparison.

Hole accumulation may also be explained by a similar mechanism reported for the pure Bi_2O_3 surface [54], involving a series of reactions and the formations of higher oxidation state of bismuth ions:

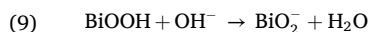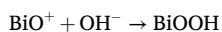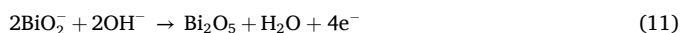$$Bi_2O_3 + 2H^+ \rightarrow 2BiO^+ + H_2O \tag{8}$$
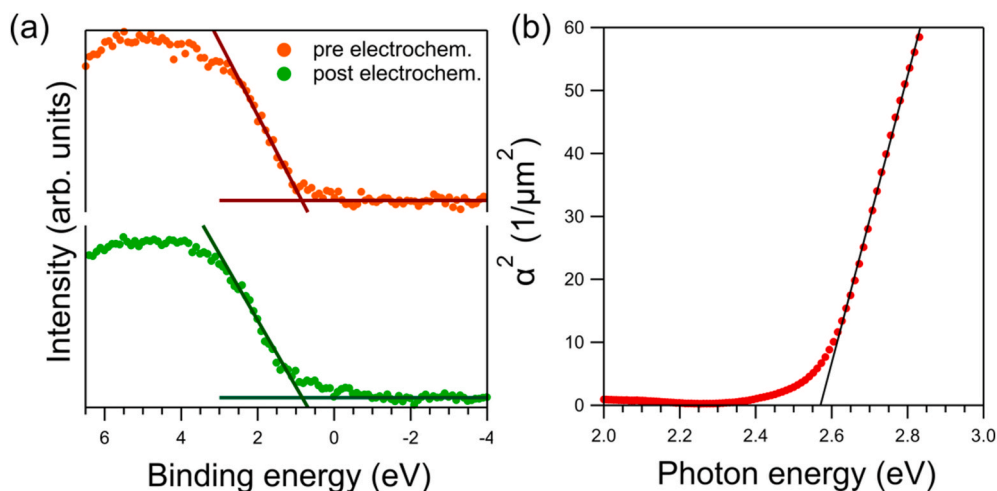
Fig. 5. (a) XPS measurement of the valence band for the BFO deposited on FTO post the annealing process (orange curve) and post the electrochemical measurement (green curve). The intercepts of the linear fit identify the position of the valence band. (b) Tauc plot of BFO on FTO glass after the annealing process with $E_g = 2.57 \pm 0.04$ eV.
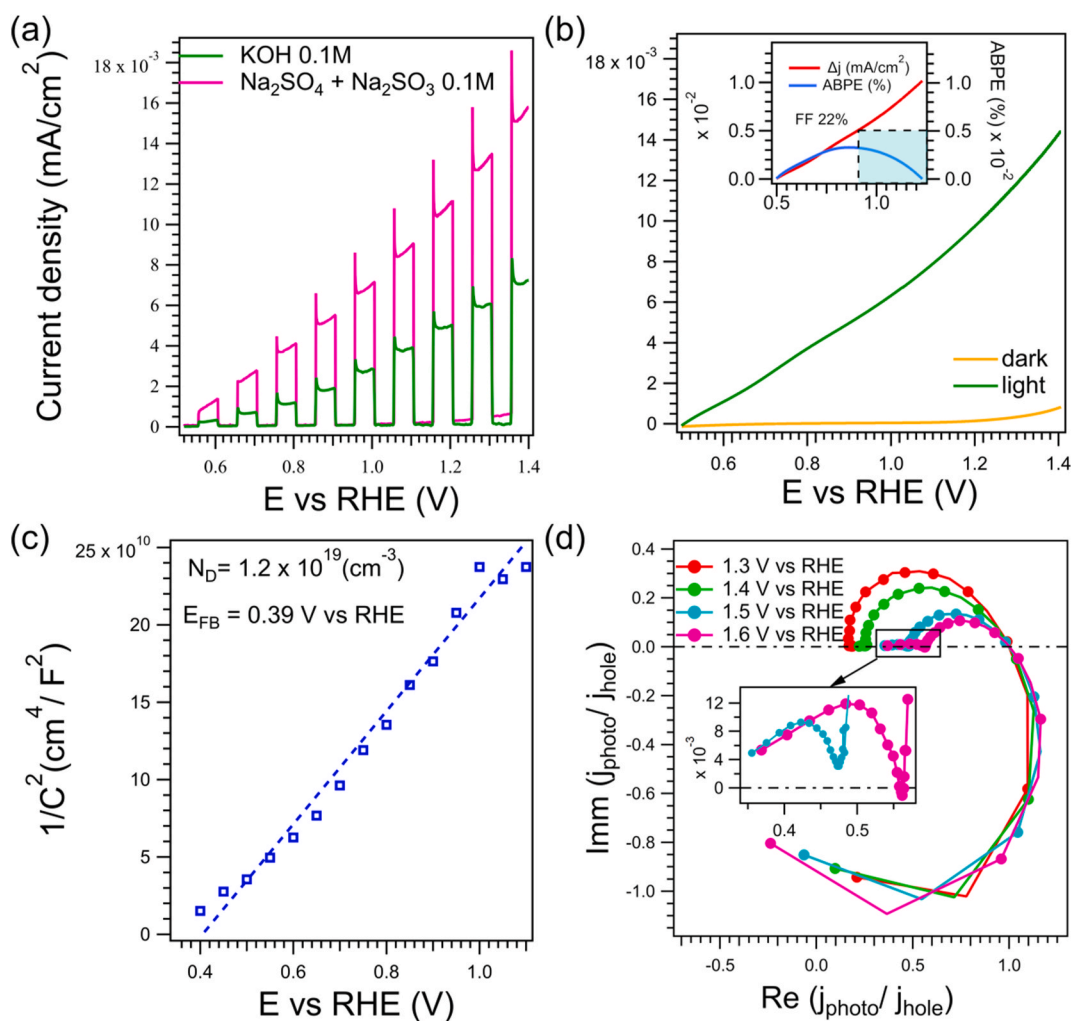
Fig. 6. (a) Chopped light LSV results obtained in 0.1 M KOH and 0.1 M Na_2SO_4 + 0.1 M Na_2SO_3; (b) LSVs in 0.1 M Na_2SO_4 + 0.1 M Na_2SO_3 in the dark and under illumination. The corresponding ABPE curve and FF value is reported in the inset; (c) MS plot and (d) normalized IMPS Nyquist plot, obtained in 0.1 M Na_2SO_4 + 0.1 M Na_2SO_3.

$$BiO^+ + OH^- \rightarrow BiOOH \qquad (9)$$

$$BiOOH + OH^- \rightarrow BiO_2^- + H_2O \qquad (10)$$

$$2BiO_2^- + 2OH^- \rightarrow Bi_2O_5 + H_2O + 4e^- \tag{11}$$

$$Bi_2O_3 + Bi_2O_5 \rightarrow 2Bi_2O_4 \tag{12}$$

In the present case, reaction 11 should imply the consumption of holes from the Bi_2O_3 valence band upon light excitation, and the measured anodic photocurrent would give rise to a self-oxidation of the material with accumulation of holes on the surface. The holes accumulation on the Bi_2O_3 surface, corresponding to Bi^{4+} surface states, is confirmed by IMPS spectra reported in Fig. 6d. IMPS is usually applied to measure in a straightforward manner the recombination kinetic constant (k_{rec}) and the charge injection constant (k_{inj}) in a photoelectrode. The separation of photogenerated charge across the depletion layer influences $\Delta\varphi_{sc}$, the potential drop within the depletion layer [56]. In the presence of surface states, this change causes the charging of the surface capacitance. The IMPS transfer function is thus modified, and the presence of high capacitance surface states is often visible in an IMPS Nyquiskt plot as a double semicircle in the 1st quadrant of the complex plane. The semi-circle at low frequency corresponds to the charging of these surface states. This process is clearly visible in Fig. 6d confirming the difficulty in the charge injection even in the case of iron-doped β-Bi_2O_3 [55]. Details about the transfer function with and without SS accumulation is reported in the supporting information (Equations a, d and Fig. S3). To minimize surface state effects and improve charge injection transfer the material was also decorated with CoPi (Cobalt phosphate) like co-catalyst. CoPi deposition however completely inactivated the photoelectrochemical performance of $Bi_{24}Fe_2O_{39}$.

In Fig. 7 we show the result of IPCE measurements between 800 and 365 nm. A 3D plot where both bias and wavelengths are varied is reported in Fig. 7a, while Fig. 7b shows the "slice" from the 3D plot at 1.23 V. The specimen presents negligible IPCE (%) values for a significant part of the spectrum, *i.e.* above ≈500 nm. For wavelengths lower than ≈500 nm the IPCE value rises, reaching 2.5 % for λ = 365 nm @ 1.23 V. Since the IPCE = $\eta_{h/e}\eta_{tr}\eta_{CT}$ [57], with $\eta_{h/e}$ = electron/hole pair generation efficiency, η_{CT} = charge injection efficiency, and η_{tr} = charge transport efficiency through the depletion layer, it is plausible that the rather low value at 1.23 V is mainly due to the scarce charge transport efficiency [57], roughly at 4 %. This value can be obtained from the IPCE value divided by $\eta_{h/e}\eta_{CT}$. Since the SS capacity at low biases is small and the "second" semi-circle is hardly visible in the IMPS plot, we cannot estimate η_{CT} for potentials lower than 1.4 V vs RHE. An η_{CT} value of about 86 % can be obtained from the IMPS plot at 1.4 V (LFI/HFI), while the absorbance photoconversion efficiency (APCE) data at 365 nm and 1.4 V vs RHE gives an $\eta_{h/e}$ value of about 82 %. k_{rec} and k_{inj}, obtained from the same portion of the plot used to calculate η_{CT}, are worth $k_{rec} =$

0.5 rad/s and k_{inj} = 3.2 rad/s (ω_{max} = 4 rad/s), respectively. The obtained value for η_{tr} agrees with the inert pair effect of Bi and the difficulty for charge transport through the material, likely related to small polaron hopping. A possible more efficient "channel" for charge transport could be through Fe ions, but a nominal amount of only 8.3 % with respect to Bi is evidently not enough to allow an optimal PEC activity.

4. Conclusions

In this paper, BFO thin films on FTO substrates, to be used as photoanodes for water splitting, were synthesized through NPs deposition by SCBD, followed by thermal annealing in air. The obtained electrodes present a nanogranular morphology with a grain size of 30 ± 2 nm and are constituted of a pure $Bi_{24}Fe_2O_{39}$ phase. The films possess a direct energy gap of 2.57 eV with a valence band edge at 0.85 eV below the Fermi level, positioned at 0.39 V vs RHE in the MS diagram. A current density of 10 μA/cm^2 at 1.23 V makes this material electrochemical performance comparable to that of β-Bi_2O_3. The data presented shows how this catalytic activity is due to the hole's accumulation at the electrode/electrolyte interface. Furthermore, the IMPS data analysis allowed to extract a charge injection efficiency of 86 % in the presence of Na_2SO_3. The low value of charge transport efficiency obtained from IMPS, IPCE and APCE analyses is explained by determining the kinetic reaction constants k_{rec} and k_{inj}, suggesting the role of small polaron hopping as limit of the PEC performances. Nevertheless, we think that its good stability in neutral or alkaline environments and especially the low E_{FB} value suggests its use as efficient photocatalyst.

CRediT authorship contribution statement

Skerxho Osmani: Data curation, Formal analysis, Investigation, Writing – original draft, Writing – review & editing. **Enrico Scattolin:** Data curation, Formal analysis, Investigation, Writing – original draft, Writing – review & editing. **Michele Vergari:** Data curation, Formal analysis, Investigation, Validation, Writing – original draft, Writing – review & editing. **Alberto Gasparotto:** Data curation, Formal analysis, Writing – original draft, Writing – review & editing. **Gian Andrea Rizzi:**
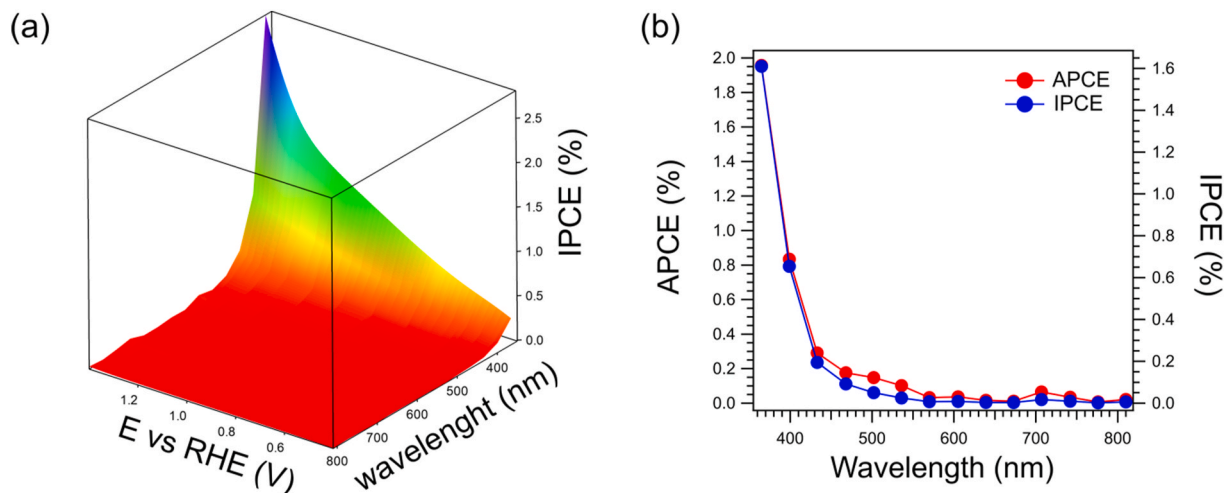
Fig. 7. (a) IPCE 3D plot collected between 800 and 365 nm. (b) Comparison between APCE (red curve) and IPCE (blue curve) values taken at 1.23V vs RHE.

Conceptualization, Data curation, Formal analysis, Funding acquisition, Investigation, Methodology, Project administration, Resources, Supervision, Validation, Writing – original draft, Writing – review & editing. **Luca Gavioli:** Conceptualization, Data curation, Formal analysis, Funding acquisition, Investigation, Methodology, Project administration, Resources, Supervision, Validation, Visualization, Writing – original draft, Writing – review & editing.

Declaration of competing interest

The authors declare that they have no known competing financial interests or personal relationships that could have appeared to influence the work reported in this paper.

Data availability

Data will be made available on request.

Appendix A. Supplementary data

Supplementary data to this article can be found online at https://doi.org/10.1016/j.jpcs.2024.112160.

References

[1] T. Baran, A. Visibile, M. Busch, X. He, S. Wojtyla, S. Rondinini, A. Minguzzi, A. Vertova, Copper oxide-based photocatalysts and photocathodes: fundamentals and recent advances, Molecules 26 (2021) 7271, https://doi.org/10.3390/molecules26237271.

[2] C. Jiang, S.J.A. Moniz, A. Wang, T. Zhang, J. Tang, Photoelectrochemical devices for solar water splitting – materials and challenges, Chem. Soc. Rev. 46 (2017) 4645–4660, https://doi.org/10.1039/C6CS00306K.

[3] Y. Man, R. Zong, Y. Zhu, Preparation and photoelectrochemical properties of Bi2MoO6 films, Acta Phys. Chim. Sin. 23 (2007) 1671–1676, https://doi.org/10.1016/S1872-1508(07)60080-1.

[4] T. Saison, P. Gras, N. Chemin, C. Chanéac, O. Durupthy, V. Brezová, C. Colbeau-Justin, J.-P. Jolivet, New insights into Bi_2WO_6 properties as a visible-light photocatalyst, J. Phys. Chem. C 117 (2013) 22656–22666, https://doi.org/10.1021/jp4048192.

[5] Y. Pihosh, I. Turkevych, K. Mawatari, J. Uemura, Y. Kazoe, S. Kosar, K. Makita, T. Sugaya, T. Matsui, D. Fujita, M. Tosa, M. Kondo, T. Kitamori, Photocatalytic generation of hydrogen by core-shell WO3/BiVO4 nanorods with ultimate water splitting efficiency, Sci. Rep. 5 (2015) 11141, https://doi.org/10.1038/srep11141.

[6] F.F. Abdi, L. Han, A.H.M. Smets, M. Zeman, B. Dam, R. Van De Krol, Efficient solar water splitting by enhanced charge separation in a bismuth vanadate-silicon tandem photoelectrode, Nat. Commun. 4 (2013) 2195, https://doi.org/10.1038/ncomms3195.

[7] Y.-S. Chen, J.S. Manser, P.V. Kamat, All solution-processed lead halide perovskite-BiVO4 tandem assembly for photolytic solar fuels production, J. Am. Chem. Soc. 137 (2015) 974–981, https://doi.org/10.1021/ja511739y.

[8] J. Jiang, M. Wang, Q. Chen, S. Shen, M. Li, L. Guo, Synthesis and characterization of nanoporous Bi3NbO7 films: application to photoelectrochemical water splitting, RSC Adv. 4 (2014) 10542–10548, https://doi.org/10.1039/C3RA47118G.

[9] N. Wang, X. Luo, L. Han, Z. Zhang, R. Zhang, H. Olin, Y. Yang, Structure, performance, and application of BiFeO3 nanomaterials, Nano-Micro Lett. 12 (2020) 81, https://doi.org/10.1007/s40820-020-00420-6.

[10] D.K. Lee, D. Lee, M.A. Lumley, K.-S. Choi, Progress on ternary oxide-based photoanodes for use in photoelectrochemical cells for solar water splitting, Chem. Soc. Rev. 48 (2019) 2126–2157, https://doi.org/10.1039/C8CS00761F.

[11] A.J.E. Rettie, W.D. Chemelewski, D. Emin, C.B. Mullins, Unravelling small-polaron transport in metal oxide photoelectrodes, J. Phys. Chem. Lett. 7 (2016) 471–479, https://doi.org/10.1021/acs.jpclett.5b02143.

[12] L. Girardi, G.A. Rizzi, L. Bigiani, D. Barreca, C. Maccato, C. Marega, G. Granozzi, Copper vanadate nanobelts as anodes for photoelectrochemical water splitting: influence of CoOx overlayers on functional performances, ACS Appl. Mater. Interfaces 12 (2020) 31448–31458, https://doi.org/10.1021/acsami.0c06915.

[13] D. Bernhardsgrütter, M.M. Schmid, Modeling of intensity-modulated photocurrent/photovoltage spectroscopy: effect of mobile ions on the dynamic response of perovskite solar cells, J. Phys. Chem. C 123 (2019) 30077–30087, https://doi.org/10.1021/acs.jpcc.9b08457.

[14] E.A. Ponomarev, L.M. Peter, A comparison of intensity modulated photocurrent spectroscopy and photoelectrochemical impedance spectroscopy in a study of photoelectrochemical hydrogen evolution at p-InP, J. Electroanal. Chem. 397 (1995) 45–52, https://doi.org/10.1016/0022-0728(95)04148-9.

[15] L.M. Peter, Dynamic aspects of semiconductor photoelectrochemistry, Chem. Rev. 90 (1990) 753–769, https://doi.org/10.1021/cr00103a005.

[16] S. Byun, G. Jung, S.-Y. Moon, B. Kim, J.Y. Park, S. Jeon, S.-W. Nam, B. Shin, Compositional engineering of solution-processed BiVO4 photoanodes toward highly efficient photoelectrochemical water oxidation, Nano Energy 43 (2018) 244–252, https://doi.org/10.1016/j.nanoen.2017.11.034.

[17] C.-M. Jiang, G. Segev, L.H. Hess, G. Liu, G. Zaborski, F.M. Toma, J.K. Cooper, I. D. Sharp, Composition-dependent functionality of copper vanadate photoanodes, ACS Appl. Mater. Interfaces 10 (2018) 10627–10633, https://doi.org/10.1021/acsami.8b02977.

[18] T.S. Sinclair, B.M. Hunter, J.R. Winkler, H.B. Gray, A.M. Müller, Factors affecting bismuth vanadate photoelectrochemical performance, Mater. Horiz. 2 (2015) 330–337, https://doi.org/10.1039/C4MH00156G.

[19] P. Sharma, M. Acharya, A. Yengantiwar, A. Gupta, Enhanced solar water splitting using bismuth ferrite photoanodes grown by direct liquid injection chemical vapor deposition, Mater. Sci. Semicond. Process. 169 (2024) 107929, https://doi.org/10.1016/j.mssp.2023.107929.

[20] S.J.A. Moniz, C.S. Blackman, P. Southern, P.M. Weaver, J. Tang, C.J. Carmalt, Visible-light driven water splitting over $BiFeO_3$ photoanodes grown via the LPCVD reaction of $[Bi(O^tBu)_3]$ and $[Fe(O^tBu)_3]_2$ and enhanced with a surface nickel oxygen evolution catalyst, Nanoscale 7 (2015) 16343–16353, https://doi.org/10.1039/C5NR04804D.

[21] A. Radmilovic, T.J. Smart, Y. Ping, K.-S. Choi, Combined experimental and theoretical investigations of n-type $BiFeO_3$ for use as a photoanode in a photoelectrochemical cell, Chem. Mater. 32 (2020) 3262–3270, https://doi.org/10.1021/acs.chemmater.0c00545.

[22] D.K. Lee, K.-S. Choi, Enhancing long-term photostability of BiVO4 photoanodes for solar water splitting by tuning electrolyte composition, Nat. Energy 3 (2018) 53–60, https://doi.org/10.1038/s41560-017-0057-0.

[23] M. Alexe, D. Hesse, Tip-enhanced photovoltaic effects in bismuth ferrite, Nat. Commun. 2 (2011) 256, https://doi.org/10.1038/ncomms1261.

[24] Q. Yu, M. Yang, X. Luo, Z. Fan, Q. Wu, Q. Zeng, Y. Li, Improving photoelectrochemical water oxidation activity of BiFeO3 photoanode via surface passivation, Appl. Phys. Lett. 119 (2021) 013903, https://doi.org/10.1063/5.0047079.

[25] W. Mao, Q. Yao, N. Liu, H. Shu, J. Zhu, Y. Pu, X. Li, Effect of Ca doping on photovoltaic effect of BiFeO3, Appl. Phys. 127 (2021) 508, https://doi.org/10.1007/s00339-021-04651-1.

[26] Z. Zhang, B. Tan, W. Ma, B. Liu, M. Sun, J.K. Cooper, W. Han, $BiFeO_3$ photocathodes for efficient H_2O_2 production via charge carrier dynamics engineering, Mater. Horiz. 9 (2022) 1999–2006, https://doi.org/10.1039/D2MH00201A.

[27] Y. Wang, M. Daboczi, C.A. Mesa, S.R. Ratnasingham, J.-S. Kim, J.R. Durrant, S. Dunn, H. Yan, J. Briscoe, $Bi_2Fe_4O_9$ thin films as novel visible-light-active photoanodes for solar water splitting, J. Mater. Chem. A 7 (2019) 9537–9541, https://doi.org/10.1039/C8TA09583C.

[28] S.A. Monny, Z. Wang, T. Lin, P. Chen, B. Luo, L. Wang, Designing efficient $Bi_2Fe_4O_9$ photoanodes via bulk and surface defect engineering, Chem. Commun. 56 (2020) 9376–9379, https://doi.org/10.1039/D0CC04455E.

[29] X. Li, X. Xiang, J. Chen, D. Jin, J. Cheng, Synthesis of highly active photocatalyst mesoporous Bi24Fe2O39 nanoparticles via a P123-assisted sol–gel method, J. Occup. Med. 74 (2022) 2783–2790, https://doi.org/10.1007/s11837-022-05214-2.

[30] E. Cavaliere, G. Benetti, M. Van Bael, N. Winckelmans, S. Bals, L. Gavioli, Exploring the optical and morphological properties of Ag and Ag/TiO2 nanocomposites grown by supersonic cluster beam deposition, Nanomaterials 7 (2017) 442, https://doi.org/10.3390/nano7120442.

[31] V. Balzano, E. Cavaliere, M. Fanetti, S. Gardonio, L. Gavioli, The role of substrate on thermal evolution of Ag/TiO2 nanogranular thin films, Nanomaterials 11 (2021) 2253, https://doi.org/10.3390/nano11092253.

[32] G. Benetti, E. Cavaliere, R. Brescia, S. Salassi, R. Ferrando, A. Vantomme, L. Pallecchi, S. Pollini, S. Boncompagni, B. Fortuni, M.J. Van Bael, F. Banfi, L. Gavioli, Tailored Ag–Cu–Mg multielemental nanoparticles for wide-spectrum antibacterial coating, Nanoscale 11 (2019) 1626–1635, https://doi.org/10.1039/C8NR08375D.

[33] M. Bottagisio, V. Balzano, L. Ciambriello, L. Rosa, G. Talò, A.B. Lovati, E. De Vecchi, L. Gavioli, Exploring multielement nanogranular coatings to forestall implant-related infections, Front. Cell. Infect. Microbiol. 13 (2023), https://doi.org/10.3389/fcimb.2023.1128822.

[34] T. Mazza, E. Barborini, I.N. Kholmanov, P. Piseri, G. Bongiorno, S. Vinati, P. Milani, C. Ducati, D. Cattaneo, A. Li Bassi, C.E. Bottani, A.M. Taurino, P. Siciliano, Libraries of cluster-assembled titania films for chemical sensing, Appl. Phys. Lett. 87 (2005) 103108, https://doi.org/10.1063/1.2035874.

[35] E. Barborini, I.N. Kholmanov, P. Piseri, C. Ducati, C.E. Bottani, P. Milani, Engineering the nanocrystalline structure of TiO2 films by aerodynamically filtered cluster deposition, Appl. Phys. Lett. 81 (2002) 3052–3054, https://doi.org/10.1063/1.1510579.

[36] L. Ciambriello, E. Cavaliere, I. Vassalini, I. Alessandri, M. Ferroni, L. Leoncino, R. Brescia, L. Gavioli, Role of electrode thickness in NiFe nanogranular films for oxygen evolution reaction, J. Phys. Chem. C 126 (2022) 21759–21770, https://doi.org/10.1021/acs.jpcc.2c06669.

[37] G. Greczynski, L. Hultman, X-ray photoelectron spectroscopy: towards reliable binding energy referencing, Prog. Mater. Sci. 107 (2020) 100591, https://doi.org/10.1016/j.pmatsci.2019.100591.

[38] J.I. Pankove, Optical Processes in Semiconductors, Unabridged Republication, with Slight Corrections, Dover Publications, Inc, New York, 1975.

[39] A.R. Zanatta, Revisiting the optical bandgap of semiconductors and the proposal of a unified methodology to its determination, Sci. Rep. 9 (2019) 11225, https://doi.org/10.1038/s41598-019-47670-y.

[40] A. Dolgonos, T.O. Mason, K.R. Poeppelmeier, Direct optical band gap measurement in polycrystalline semiconductors: a critical look at the Tauc method, J. Solid State Chem. 240 (2016) 43–48, https://doi.org/10.1016/j.jssc.2016.05.010.

[41] P. Milani, S. Iannotta, Cluster Beam Synthesis of Nanostructured Materials, Springer, Berlin Heidelberg New York Barcelona Budapest Hong Kong London Milan Paris Singapore Tokyo, 1999.

[42] F. Borghi, A. Podestà, C. Piazzoni, P. Milani, Growth mechanism of cluster-assembled surfaces: from submonolayer to thin-film regime, Phys. Rev. Appl. 9 (2018) 044016, https://doi.org/10.1103/PhysRevApplied.9.044016.

[43] X.H. Zhu, E. Defaÿ, Y. Lee, B. André, M. Aïd, J.L. Zhu, D.Q. Xiao, J.G. Zhu, High permittivity Bi24Fe2O39 thin films prepared by a low temperature process, Appl. Phys. Lett. 97 (2010) 232903, https://doi.org/10.1063/1.3524492.

[44] N. Asefi, S.M. Masoudpanah, M. Hasheminiasari, Photocatalytic performances of BiFeO3 powders synthesized by solution combustion method: the role of mixed fuels, Mater. Chem. Phys. 228 (2019) 168–174, https://doi.org/10.1016/j.matchemphys.2019.02.059.

[45] D. Karoblis, D. Griesiute, K. Mazeika, D. Baltrunas, D.V. Karpinsky, A. Lukowiak, P. Gluchowski, R. Raudonis, A. Katelnikovas, A. Zarkov, A. Kareiva, A facile synthesis and characterization of highly crystalline submicro-sized BiFeO3, Materials 13 (2020) 3035, https://doi.org/10.3390/ma13133035.

[46] T. Pikula, T. Szumiata, K. Siedliska, V.I. Mitsiuk, R. Panek, M. Kowalczyk, E. Jartych, The influence of annealing temperature on the structure and magnetic properties of nanocrystalline BiFeO3 prepared by sol–gel method, Metall. Mater. Trans. A 53 (2022) 470–483, https://doi.org/10.1007/s11661-021-06506-z.

[47] T.I. Mel'nikova, G.M. Kuz'micheva, N.B. Bolotina, V.B. Rybakov, YaV. Zubavichus, N.V. Sadovskaya, E.A. Mar'ina, Structural features of compounds of the sillenite family, Crystallogr. Rep. 59 (2014) 353–361, https://doi.org/10.1134/S1063774514030134.

[48] J. Dzik, A. Lisinska-Czekaj, A. Zarycka, D. Czekaj, Study of phase and chemical composition of Bi1-xNdxFeO3 powders derived by pressureless sintering, Arch. Metall. Mater. 58 (2013) 1371–1376, https://doi.org/10.2478/amm-2013-0177.

[49] Arushi Arora, Ritika Wadhwa, Krishna K. Yadav, Ankush, Menaka Jha, Enhanced electrochemical oxygen generation from sillenite phase of bismuth iron oxide (Bi24Fe2O39) ultrafine particles stabilised at room temperature, J. Electroanal. Chem. 958 (2024) 118154, https://doi.org/10.1016/j.jelechem.2024.118154.

[50] G.A. Gomez-Iriarte, A. Pentón-Madrigal, L.A.S. De Oliveira, J.P. Sinnecker, XPS study in BiFeO3 surface modified by argon etching, Materials 15 (2022) 4285, https://doi.org/10.3390/ma15124285.

[51] G. Bhargava, I. Gouzman, C.M. Chun, T.A. Ramanarayanan, S.L. Bernasek, Characterization of the "native" surface thin film on pure polycrystalline iron: a high resolution XPS and TEM study, Appl. Surf. Sci. 253 (2007) 4322–4329, https://doi.org/10.1016/j.apsusc.2006.09.047.

[52] J.L. Ortiz-Quiñonez, C. Vega-Verduga, D. Díaz, I. Zumeta-Dubé, Transformation of bismuth and β-Bi2O3 nanoparticles into (BiO)2CO3 and (BiO)4(OH)2CO3 by capturing CO2: the role of halloysite nanotubes and "sunlight" on the crystal shape and size, Cryst. Growth Des. 18 (2018) 4334–4346, https://doi.org/10.1021/acs.cgd.8b00177.

[53] Y. Huang, W. Wang, Q. Zhang, J. Cao, R. Huang, W. Ho, S.C. Lee, In situ fabrication of α-Bi2O3/(BiO)2CO3 nanoplate heterojunctions with tunable optical property and photocatalytic activity, Sci. Rep. 6 (2016), https://doi.org/10.1038/srep23435.

[54] K.C. Chitrada, R. Gakhar, D. Chidambaram, E. Aston, K.S. Raja, Enhanced performance of β-Bi2O3 by in-situ photo-conversion to Bi2O3-BiO2-x composite photoanode for solar water splitting, J. Electrochem. Soc. 163 (2016) H546–H558, https://doi.org/10.1149/2.0721607jes.

[55] A. Vijay, K.V. Ramanujachary, S.E. Lofland, S. Vaidya, Role of crystal structure and electrical polarization of an electrocatalyst in enhancing oxygen evolution performance: Bi-Fe-O system as a case study, Acta 407 (2022) 139887, https://doi.org/10.1016/j.electacta.2022.139887.

[56] E.A. Ponomarev, L.M. Peter, A generalized theory of intensity modulated photocurrent spectroscopy (IMPS), J. Electroanal. Chem. 396 (1995) 219–226, https://doi.org/10.1016/0022-0728(95)04115-5.

[57] Z. Chen, H.N. Dinh, E. Miller, Photoelectrochemical Water Splitting: Standards, Experimental Methods, and Protocols, Springer, New York, New York, NY, 2013, https://doi.org/10.1007/978-1-4614-8298-7.